

Molecular dynamics study incorporating regression analysis: Quantitative effects of sinusoidal protrusions and wettability on water phase transition containing insoluble gases

Bingheng Li(李丙衡), Yujian Gao(高雨键), Mian Yu(余绵), Lianfeng Wu(吴连锋), Lianxiang Ma(马连湘), and Yuanzheng Tang(唐元政)

Citation: Chin. Phys. B, 2025, 34 (**11**): 114704. DOI: 10.1088/1674-1056/ae0894
http://cpb.iphy.ac.cn; http://iopscience.iop.org/cpb

What follows is a list of articles you may be interested in

Stable nanobubbles on ordered water monolayer near ionic model surfaces

Luyao Huang(黄璐瑶), Cheng Ling(凌澄), Limin Zhou(周利民), Wenlong Liang(梁文龙), Yujie Huang(黄雨婕), Lijuan Zhang(张立娟), Phornphimon Maitarad, Dengsong Zhang(张登松), and Chunlei Wang(王春雷)
Chin. Phys. B, 2025, 34 (**1**): 014701. DOI: 10.1088/1674-1056/ad989d

Molecular dynamics simulation of the flow mechanism of shear-thinning fluids in a microchannel

Gang Yang(杨刚), Ting Zheng(郑庭), Qihao Cheng(程启昊), and Huichen Zhang(张会臣)
Chin. Phys. B, 2024, 33 (**4**): 044701. DOI: 10.1088/1674-1056/ad08a7

A study of cavitation nucleation in pure water using molecular dynamics simulation

Hua Xie(谢华), Yuequn Xu(徐跃群), and Cheng Zhong(钟成)
Chin. Phys. B, 2022, 31 (**11**): 114701. DOI: 10.1088/1674-1056/ac588a

Molecular dynamics simulations on the wet/dry self-latching and electric fields triggered wet/dry transitions between nanosheets: A non-volatile memory nanostructure

Jianzhuo Zhu(朱键卓), Xinyu Zhang(张鑫宇), Xingyuan Li(李兴元), and Qiuming Peng(彭秋明)
Chin. Phys. B, 2022, 31 (**2**): 024703. DOI: 10.1088/1674-1056/ac3811

Comparative investigation of microjetting generated from monocrystalline tin surface and polycrystalline tin surface under plane impact loading

Shao-Wei Sun(孙少伟), Guan-Qing Tang(汤观晴), Ya-Fei Huang(黄亚飞), Liang-Zhi Cao(曹良志), and Xiao-Ping Ouyang(欧阳晓平)
Chin. Phys. B, 2021, 30 (**10**): 104701. DOI: 10.1088/1674-1056/abeeea

---

SPECIAL TOPIC — Heat conduction and its related interdisciplinary areas

Molecular dynamics study incorporating regression analysis: Quantitative effects of sinusoidal protrusions and wettability on water phase transition containing insoluble gases

Bingheng Li(李丙衡)[1], Yujian Gao(高雨键)[1], Mian Yu(余绵)[1], Lianfeng Wu(吴连锋)[2], Lianxiang Ma(马连湘)[1], and Yuanzheng Tang(唐元政)[1,†]

[1] *College of Electromechanical Engineering, Qingdao University of Science and Technology, Qingdao* 266061, *China*
[2] *State Key Laboratory of Marine Coatings, Marine Chemical Research Institute Co., Ltd., Qingdao* 266071, *China*

(Received 1 July 2025; revised manuscript received 17 September 2025; accepted manuscript online 18 September 2025)

Molecular dynamics simulations were employed to establish a more realistic model of nanoscale boiling phase transitions. We examined the effects of different configurations of nanoscale sinusoidal protrusions and surface wettability on the phase transition behavior of systems containing insoluble gases under continuous heat flux input. To enhance the clarity and comparability of the results, a quantitative evaluation method was introduced. The findings reveal that, under identical wettability conditions, increasing the number of sinusoidal protrusions accelerates the onset of phase transition. In contrast, for a fixed number of protrusions, higher surface wettability delays the initiation of the phase change. By incorporating regression analysis to quantify the phase transition process and compare influencing factors, it was observed that although high wettability generally inhibits phase transition, the synergistic interaction between surface structure and wettability ultimately facilitates the phase transition process.

Keywords: molecular dynamics, boiling, heat flux, insoluble gas

PACS: 47.55.dp, 44.20.+b, 44.90.+c, 83.10.Mj

DOI: 10.1088/1674-1056/ae0894 **CSTR:** 32038.14.CPB.ae0894

1. Introduction

Boiling heat transfer has attracted wide attention in both fundamental and practical studies due to its highly efficient heat transfer performance. A massive amount of heat can be transferred rapidly because of the latent heat released during the boiling phase change process. Boiling is intrinsically a microscopic phenomenon involving bubble behavior at the micro- and nanoscale. Meanwhile, with the continuous miniaturization of electronic devices and the increasing precision of industrial production, boiling at the micro- and nanoscale has recently become a research hotspot.

Traditional experimental approaches and macroscopic continuum models are limited in their ability to investigate nanoscale phenomena, as their analyses are hindered by size effects and often yield unsatisfactory results. As a powerful tool for studying nanoscale phase-change heat transfer, molecular dynamics (MD) simulations enable detailed exploration of microscale processes and allow for a more accurate analysis of the underlying mechanisms. For example, Chen *et al.*[1] demonstrated that nanostructured surfaces can enhance both heating efficiency and nucleation rates by increasing the solid–liquid contact area and introducing surface temperature inhomogeneities. Their results showed that heat flux density increases with the height of the nanostructures. Similarly, Hajebzadeh *et al.*[2] reported that tree-root-shaped structures improved the evaporation rate, maximum heat flux density, and convective heat transfer coefficient. Zhang *et al.*[3] compared explosive boiling on three different surface structures, revealing that surface morphology significantly affects the phase transition rate. She *et al.*[4] found that nanostructures provide a larger effective volume for liquid argon, which reduces the relative gas density and accelerates bubble nucleation and phase change. Hong *et al.*[5] and Dong *et al.*[6] combined experimental studies with numerical simulations and showed that concave surface features enhance phase-change heat transfer at the microscale. Seyf and Zhang[7] systematically investigated the boiling eruption of a thin liquid film using conical nanostructures. Their results indicated that such structures enhance solid–liquid heat transfer and influence the temperature at which the liquid separates from the substrate, although the material composition of the nanostructures had little effect. Yin *et al.*[8] introduced nanoparticle deposition into phase-change studies and demonstrated that nanoparticle layers can improve heat transfer efficiency between liquid and solid surfaces. Huang *et al.*[9] and Esfe *et al.*[10] examined the use of nanofluids and found that heat transfer performance is influenced by the volume fraction of nanoparticles, thermal conductivity, and solid volume fraction. They also noted that the

†Corresponding author. E-mail: tangyuanzheng@163.com

© 2025 Chinese Physical Society and IOP Publishing Ltd. All rights, including for text and data mining, AI training, and similar technologies, are reserved.

thermal conductivity of nanofluids is temperature-dependent. Nagayama[11,12] focused on blistering behavior at solid–liquid interfaces to further investigate heat and mass transfer mechanisms. Chen *et al.*[13,14], Liu and Liu,[15], and Hens *et al.*[16] explored composite surfaces featuring nanostructures and non-uniform wettability, and studied bubble nucleation dynamics on such surfaces. Their findings showed that, for the same surface area, nanostructured surfaces possess greater vertical hydrophilic area compared to smooth ones, thereby enhancing nucleate boiling performance.

To date, extensive MD studies have been conducted at the atomic scale on boiling heat transfer. However, the phenomena and mechanisms of boiling heat transfer at the micro- and nanoscale are still not fully understood in several key aspects. Firstly, liquids in real-world and industrial applications often contain insoluble gases, which can significantly influence the phase transition process and bubble dynamics, thereby altering boiling heat transfer performance.[17,18] Wu and our research group[19] investigated the effect of insoluble nitrogen on the boiling behavior of liquid nanofilms on copper surfaces at various temperatures, and found that the presence of nitrogen can enhance boiling. Secondly, the boiling of liquid on a solid surface with continuous protrusions composed of sinusoidal waves has not yet been studied. The sinusoidal curve has the particular characteristic that the area enclosed by it and a horizontal line does not change with the sinusoidal period. Surfaces with sinusoidally continuous protrusions built in this work ensure that both the volume of the heated substrate and the total volume of vapor bubbles remain constant, which may provide a more accurate representation of bubble behavior. Thirdly, the temperature gradient is the primary driving force behind heat transfer and boiling. To establish a more rational temperature gradient and ensure the comparability and reproducibility of phase transition behavior, this study employs a continuous heat input method. This approach effectively eliminates complex boundary effects caused by transient heat flux variations, thereby highlighting the core research focus. To deepen the understanding of nanoscale boiling, this work simultaneously considers the effects of nitrogen, nanostructures, and wettability. Lastly, a weighted analysis of these influencing factors was conducted to determine their reinforcing or weakening effects, as well as whether synergistic enhancement exists. This provides practical guidance for understanding and improving nanoscale boiling heat transfer in engineering applications.

2. Simulation methods

A total of 15 simulation models were constructed in this study, each designed with varying surface wettability and nanoscale sinusoidal structures. Copper (Cu) atoms, water (H_2O) molecules, and nitrogen (N_2) molecules were modeled using a face-centered cubic (FCC) lattice, the simple point charge (SPC/E) model, and the OPLS-AA/L force field, respectively. A copper substrate was placed at the bottom of the simulation domain, while a copper control plate was positioned at the top. An aqueous nanofilm containing insoluble nitrogen gas was placed atop the bottom copper substrate. The detailed simulation setup is illustrated in Fig. 1, which features five sinusoidal nanostructures constructed on the substrate surface. These nanostructures were generated based on the following mathematical expression as a function of the coordinate in the x-direction

$$f(x) = h_0 + A\sin\left(\frac{2\pi x}{p}\right), \tag{1}$$

where h_0 represents the distance from the z-axis, A is the amplitude, p is the period of the sinusoidal function, and $f(x)$ is the actual coordinate in the z-direction.[20] Unlike discrete nanostructures such as protrusions or grooves, sinusoidal continuous protrusions exhibit periodicity and geometric consistency, maintaining a constant surface envelope area across different periods. This characteristic ensures that the ratio of the substrate's total volume to the bubble generation volume remains stable when altering the structural period, thereby more closely approximating the thermomechanical conditions encountered by real engineering surfaces. Five distinct sinusoidal protrusion conditions were designed, with surface roughness increasing as the period p increases. For all roughness conditions, the number of water molecules was fixed at 6679, the number of nitrogen molecules at 60, and the number of copper atoms at 4536. The sinusoidal nanostructures extend continuously along the y-direction of the simulation cell. For more detailed information regarding the simulation setup, refer to our previous studies.[19,21]

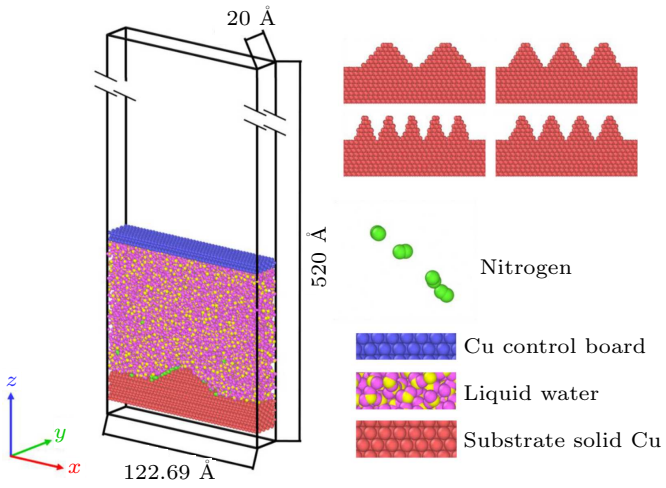


Fig. 1. The simulation system.

The interactions between Cu atoms are modeled using the embedded atom method (EAM).[22] The SPC/E water model

is adopted for its computational efficiency and reasonable accuracy in simulating water behavior.[23,24] To enhance stability and computational efficiency, the O–H bond lengths and H–O–H bond angles are constrained using the SHAKE algorithm, which prevents intramolecular vibrations during the simulation.[25] Partial charges are assigned as $q_{\mathrm{O}} = -0.8476e$ and $q_{\mathrm{H}} = 0.423e$ for the oxygen and hydrogen atoms, respectively. Long-range electrostatic interactions are calculated using the particle–particle particle–mesh (PPPM) method.[26] In the rigid SPC/E model, intermolecular forces between water molecules are primarily represented through the interactions between oxygen atoms. For nitrogen (N_2) molecules, both intra- and intermolecular interactions are parameterized using the OPLS-AA/L force field.[27,28] Interactions between different molecular species (e.g., water–nitrogen or water–copper) are described by van der Waals forces,[29] modeled using the 12–6 Lennard–Jones (LJ) potential, given by the following equation:

$$\Phi_{(r_{ij})} = \begin{cases} 4\varepsilon\left[\left(\frac{\sigma}{r_{ij}}\right)^{12} - \left(\frac{\sigma}{r_{ij}}\right)^{6}\right], & r \le r_{\mathrm{cut}}, \\ 0, & r > r_{\mathrm{cut}}, \end{cases} \tag{2}$$

where ε is the energy parameter, σ is the distance parameter, r_{ij} is the distance between atoms i and j, and r_{cut} is the cutoff radius. The van der Waals interactions between Cu–H_2O, H_2O–N_2, and Cu–N_2 are represented by the atomic pairs Cu–O, O–N, and Cu–N, respectively. Wettability plays a critical role in the boiling heat transfer of liquids on solid surfaces. In molecular dynamics simulations, wettability is typically modulated by adjusting the intermolecular interaction strength at the solid–liquid interface. This underscores the importance of accurately defining the interaction between Cu and H_2O to correctly simulate the boiling behavior of liquid water on a heated copper substrate.[29] In this study, the wettability condition is determined by the intermolecular force between Cu and H_2O and is calculated using the following equations:

$$\Phi_{(r_{ij})} = 4\varepsilon'\left[\left(\frac{\sigma'}{r}\right)^{12} - \left(\frac{\sigma'}{r}\right)^{6}\right], \tag{3}$$

$$\varepsilon' = \varepsilon\alpha = \varepsilon\beta^2, \tag{4}$$

$$\sigma' = \alpha^{-1/12}\sigma = \beta^{-1/6}\sigma, \tag{5}$$

where α and β are used to regulate the interfacial wettability conditions, while σ' and ε' represent the new length and energy parameters of the LJ potential, respectively. The potential energy parameters used in this study are summarized in Table 1.

To balance the system pressure, piston-assisted pressure control was implemented in the simulation.[30] The upper copper plate was modeled as a movable piston, with an external force applied in the z-direction to each of its atoms. This setup helps to minimize pressure fluctuations during the simulation, thereby improving the stability and accuracy of the heat and mass transfer calculations. The external force applied is computed using the following equation:

$$F_{\mathrm{atom}} = \frac{F_{\mathrm{total}}}{N_{\mathrm{up}}} = \frac{PS_{xoy}}{N_{\mathrm{up}}}, \tag{6}$$

where F_{atom} is the total force applied to the upper copper plate, N_{up} is the number of atoms in the upper copper plate, $P = 1$ bar is the target pressure, and S_{xoy} represents the cross-sectional area in the x–y plane.

Table 1. Parameters of H_2O, Cu molecules

Atom pairs	α	σ (nm)	ε (meV)
Cu–Cu	–	0.2377	409.3
O–O	–	0.3166	6.739
O–Cu (hydrophobic)	0.5	0.3380	3.685
O–Cu (neutral)	1	0.3190	7.370
O–Cu (hydrophilic)	2	0.3011	14.740
Cu–N	–	0.2788	4.981

The simulation comprises two main stages: the relaxation phase and the heating process. For each simulation cell, the initial structure was first equilibrated in a canonical (NVT) ensemble for 1 ns to achieve thermodynamic equilibrium at 298 K and 1 atm. Periodic boundary conditions were applied in all directions. The saturated mole fraction solubility of nitrogen in water at 298 K and 1 atm is approximately 1.2×10^{-5} mol/mol.[31] Based on the system dimensions, the number of N_2 molecules that can dissolve in water is less than one, indicating that the inserted N_2 molecules remain in the gas phase and are therefore considered insoluble.

After equilibration, some N_2 molecules adsorb onto the copper surface, while a few remain dispersed within the water. Following the NPT and NVT equilibration steps, the simulation proceeds using a microcanonical (NVE) ensemble. During this phase, the outermost Cu atoms at the bottom of the substrate are fixed to prevent displacement or penetration through the z-boundary. To maintain structural integrity, an elastic force[32] is applied to the non-fixed Cu atoms at the bottom, allowing them to oscillate around their equilibrium positions and preventing structural collapse. The applied force is defined as

$$F = \frac{Kr^2}{2}, \tag{7}$$

where $K = 52$ eV·Å^{-2} is the elastic constant, and r represents the displacement of atoms from their initial positions. As illustrated in Fig. 1, a total of 4032 copper atoms (corresponding to six atomic layers) near the fixed region at the bottom substrate were designated as heat sources, where a constant heat flux was applied. Our previous study[21] demonstrated that the magnitude of the substrate heat flux significantly affects boiling heat transfer performance. Based on that finding, the

current simulation adopts a more suitable and physically reasonable heat flux condition, namely, $q = 1.0 \times 10^{10}$ J·m^{-2}·s^{-1}. This heat flux ensures observable variations in boiling behavior among different systems while maintaining a manageable simulation time.

The temperature is calculated using

$$\mathrm{DOF} \cdot \frac{1}{2} K_{\mathrm{B}} T = \sum_{i=1}^{N} \frac{1}{2} m_i \boldsymbol{v}_i^2, \tag{8}$$

where DOF is the degree of freedom of the system, K_{B} is the Boltzmann constant, and m_i and $\boldsymbol{v}_i$ are the mass and velocity of atom i, respectively. For rigid H_2O molecules, each molecule has six degrees of freedom (three translational and three rotational). Therefore, to correctly compute the temperature of water, the degrees of freedom should be set as DOF $= 2N$, where N is the total number of atoms. For systems such as copper and nitrogen without any constraints or freezing, the degrees of freedom are set as DOF $= 3N$.

All molecular dynamics (MD) simulations were conducted using the large-scale atomic/molecular massively parallel simulator (LAMMPS).[30] The classical Newtonian equations of motion for each atom were solved using the velocity Verlet algorithm, with a time step of 1 femtosecond (fs). Visualization of the simulation results was performed using open visualization tool (OVITO)[33] and visual molecular dynamics (VMD).[34]

2.1. Results and discussion

To facilitate the analysis of phase-change heat transfer across different simulation systems (with varying wettability and nanostructures), Fig. 2 presents snapshots of atomic distributions along the y-direction at selected time points for each system. During the heat flux input phase, the insoluble gas within the nanoliquid film begins to migrate downward from the liquid layer and gradually approaches the surface of the copper substrate.

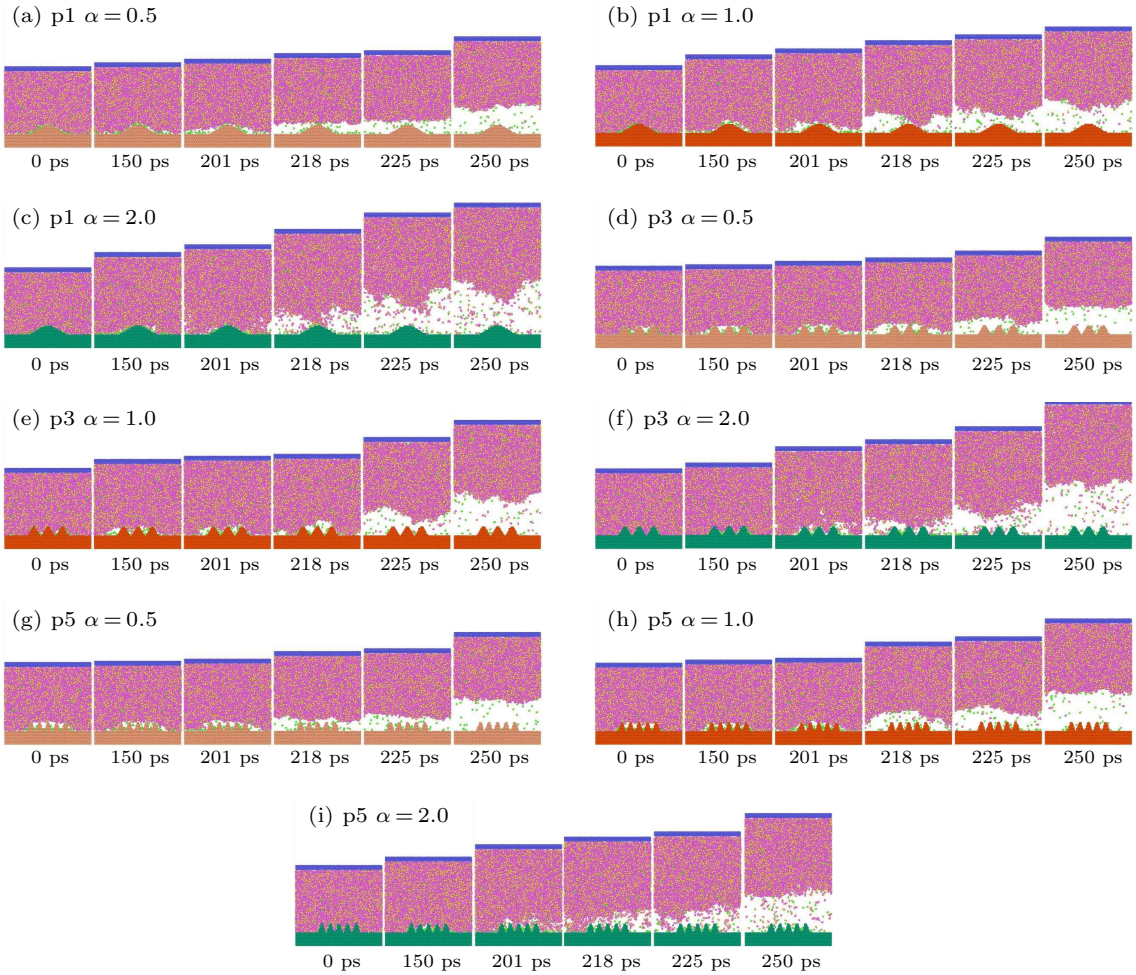


Fig. 2. Snapshot of the distribution of atoms in the y-direction.

All simulated systems exhibited burst boiling behavior. As surface wettability increased, the onset of bubble formation was delayed, and the resulting bubble volume became larger. Additionally, under the same wettability condition, a greater number of nanostructure protrusions led to an earlier onset of bubble generation. To facilitate further analysis and comparison, Table 2 summarizes the boiling onset times and liquid-film detachment times across different simulation sys-

tems. For comparison, simulation results excluding nitrogen are not presented here but can be found in other studies conducted by our research group. These findings collectively indicate that the presence of nitrogen generally promotes the initiation of phase transition. However, when nitrogen and wettability coexist, wettability becomes a limiting factor in the phase-change process. The last two columns of Table 2 show (i) the time required for the top control plate to reach a specific height under different simulation conditions, and (ii) the height of the top plate at a fixed time across systems — both used for subsequent regression analysis.

To further investigate the phase-transition process, the simulation domain is uniformly divided into blocks of equal height along the z-direction, and the average density of each block is calculated and recorded in real time. For statistical analysis, a region extending 10 Å above the bottom copper surface is selected, as shown in Fig. 3. This region is chosen because it encompasses the primary area where the phase transition occurs under the given simulation conditions. Representative statistical results are also illustrated in the figure. Initially, the density in this region remains stable. As heat input begins, the local density starts to decrease due to increasing intermolecular distances. The onset of strong density fluctuations marks the beginning of the phase transition. Furthermore, with increasing hydrophilicity, the average density in this region tends to be higher. This is attributed to the stronger attractive forces provided by hydrophilic surfaces, which draw liquid molecules closer and result in higher local liquid density. After the liquid film detaches, additional fluctuations are observed, caused by vapor molecules intermittently entering and leaving the region.

Table 2. Simulation results.

Wettability	Number of protrusions	Starting to bubble (ps)	Disengagement time (ps)	Time to reach the same height (289.1 Å) (ps)	Same time to height (710 ps) (Å)
Hydrophobic $\alpha = 0.5$	1	402	454	710	289.10
	2	384	498	753	257.08
	3	352	450	709	289.51
	4	254	364	618	365.68
	5	236	338	579	412.59
Neutral $\alpha = 1.0$	1	546	624	824	200.77
	2	514	582	795	219.48
	3	408	554	744	259.29
	4	286	472	659	341.28
	5	258	430	643	353.73
Hydrophilic $\alpha = 2.0$	1	592	682	786	211.37
	2	532	616	747	249.11
	3	454	544	687	312.98
	4	414	486	607	425.66
	5	372	414	551	508.63

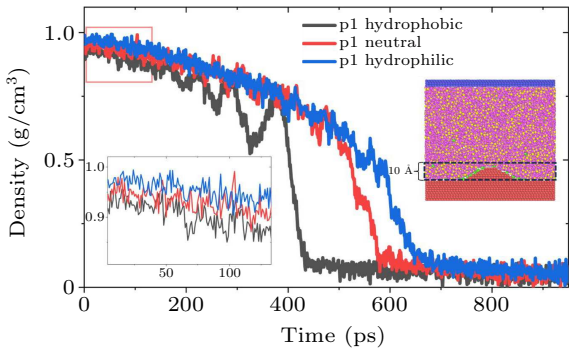


Fig. 3. Bottom region selection and bottom water molecule density change.

Nitrogen molecules are initially adsorbed onto the surface of the copper substrate, and under certain simulation conditions, the number of adsorbed nitrogen molecules increases at the onset of heat flux input. Figure 4 illustrates the variation in the number of nitrogen molecules adsorbed on the copper surface under selected conditions. A monolayer nitrogen layer is formed through van der Waals interactions between copper atoms and nitrogen molecules,[35,36] which gradually detaches from the copper surface as the heat flux increases. The maximum number of adsorbed nitrogen molecules varies with surface wettability. Under identical nanostructure conditions, hydrophilic surfaces exhibit the highest number of adsorbed nitrogen molecules. This behavior can be attributed to the enhanced stability of the interfacial water layer on hydrophilic surfaces, where water molecules tend to form a more ordered and denser structure with longer hydrogen-bond retention times.[37]

Although O–N interactions are longer-ranged, the stronger short-range interaction between Cu and N indicates that Cu–N forces play a dominant role in adsorption at close distances. Once surface water molecules acquire sufficient kinetic energy to desorb from the copper substrate, additional

adsorption sites are exposed for nitrogen molecules. The dynamic motion of water molecules further promotes nitrogen adsorption on the copper surface.[38,39] Moreover, due to their diatomic nature, nitrogen molecules possess higher adsorption energy than water molecules, resulting in delayed desorption. Consequently, nitrogen molecules remain adsorbed for longer periods and only completely detach from the substrate as the heat flux continues to increase.

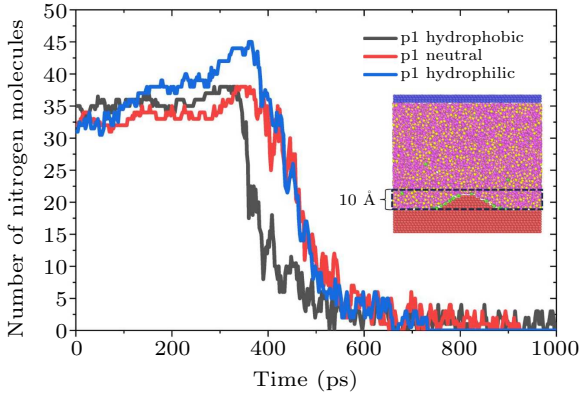


Fig. 4. Number of surface nitrogen molecules.

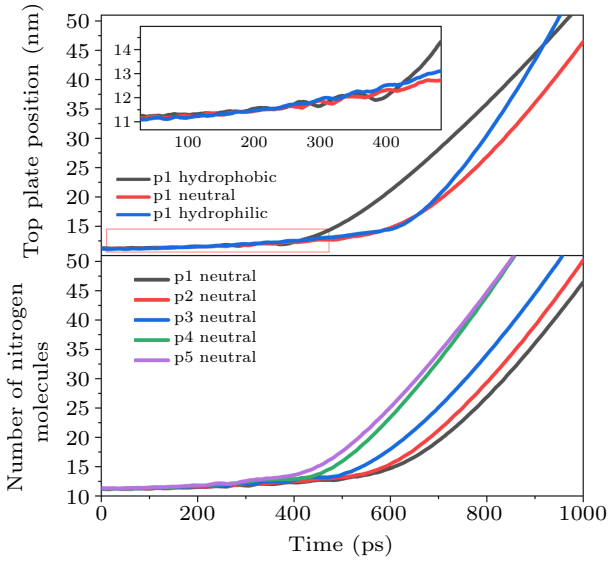


Fig. 5. Change in displacement of the top control platen.

This study also tracked the height of the top plate over time for different simulation systems. The displacement of the top plate serves as a clear indicator of the overall spatial evolution during the phase-transition process, including bubble growth and liquid-film movement. Due to the large volume of data, only a subset of representative results is presented in Fig. 5 for analysis. The entire process can be divided into three distinct stages: continuous heating, bubble growth, and vapor-film detachment. Initially, the bottom copper plate continuously transfers heat to the liquid region, triggering the formation of bubbles. As heat input continues, the bubbles grow and eventually coalesce to form a vapor film that detaches uniformly from the substrate.

As shown in Fig. 5, the number of nanoscale sinusoidal protrusions significantly affects the timing of top-plate movement. Systems with a greater number of protrusions exhibit earlier plate motion, indicating that increased surface structuring promotes earlier nucleation and accelerates the phase-transition process by providing additional nucleation sites. At later stages, the faster rise rate and steeper displacement slope of the top plate under hydrophilic conditions may be attributed to two factors. First, hydrophilic surfaces tend to suppress early bubble nucleation; when the liquid reaches a higher degree of superheat, bubbles suddenly form and grow rapidly, leading to an abrupt increase in top-plate movement.[40] Second, more heat is stored in the liquid near the hydrophilic surface during the early phase, which further accelerates the phase transition and enhances the upward motion of the top plate.

To further investigate and explain the observed phenomena, the temporal and spatial variations in temperature and density were analyzed. The simulation domain was divided along the y-direction into strips measuring 10.4 Å in height and 12.2 Å in width. The average temperature and density within each strip were computed every 100 ps, and the results were recorded accordingly. Figure 6 presents snapshots of selected simulation conditions at key time points. It is evident that vapor films on hydrophobic surfaces tend to be flatter, whereas those on hydrophilic and neutral surfaces exhibit more irregular morphologies. This suggests that hydrophobic surfaces exhibit weaker interactions with the liquid, encouraging detachment and promoting evaporation. In contrast, hydrophilic surfaces tend to retain the liquid, and the evaporation process is influenced by liquid replenishment and interfacial tension. These factors result in vapor films with unstable shapes and non-uniform thickness.

Furthermore, an increased number of sinusoidal protrusions reduces the energy barrier for bubble nucleation by providing more cavities and points of curvature discontinuity, thereby lowering the critical energy required for localized nucleation. At the same time, the enhanced surface structure introduces additional interfacial perturbations and fluid instabilities, which facilitate liquid renewal and promote the sustained progress of phase transition. In this study, the reference density of liquid water is taken as 0.75 g/cm^3.[41,42]

The overall density near hydrophilic surfaces is relatively low. This is because the stronger interaction between the hydrophilic surface and the liquid causes water molecules to remain on the surface for a longer time, absorbing more energy in the process. As a result, the water molecules attain higher energy levels and exhibit larger intermolecular spacing. In regions with intense phase-change activity, the gas–liquid interface becomes more diffuse. Most of the phase transition occurs along the sides of the sinusoidal protrusions, where rapid

curvature changes exist. These high-curvature regions are more likely to generate localized low-pressure zones, which facilitate the conversion of liquid water into vapor and reduce the energy barrier for phase change.[43]

Nitrogen, as an insoluble gas, does not directly participate in the phase transition. However, in areas such as nanostructured grooves and ribbed sidewalls — where local fluid disturbances are minimal — nitrogen molecules tend to accumulate and form stable nanogas clusters. As temperature rises, these nitrogen clusters can act as nucleation cores, lowering the energy barrier for bubble formation. Furthermore, nitrogen molecules inhibit the reaggregation of surrounding water molecules, stabilizing nascent vapor bubbles and preventing them from collapsing back into the liquid. This results in a smoother and more sustained phase-transition process. Figure 7 presents the spatiotemporal temperature distributions under different simulation conditions. The results show that the copper substrate acts as the primary heat source, maintaining a stable surface temperature above 600 K. Heat is transferred from the copper substrate to the liquid interface, where localized overheating occurs at the top of protrusions and along rib sidewalls, promoting bubble nucleation.

As the number of protrusions increases, the heat-transfer pathways become more complex, and the phase-transition zone expands from a localized to a continuous region. With increasing surface wettability, liquid adhesion is enhanced, resulting in significant heat accumulation. However, enhanced wettability also destabilizes the vapor film, whereas hydrophobic surfaces favor the formation of continuous vapor layers and facilitate the detachment of the liquid film. Additionally, the nano-liquid film exhibits a pronounced vertical temperature gradient, with lower temperatures near the top and higher temperatures near the bottom, which is consistent with previous findings.[17]

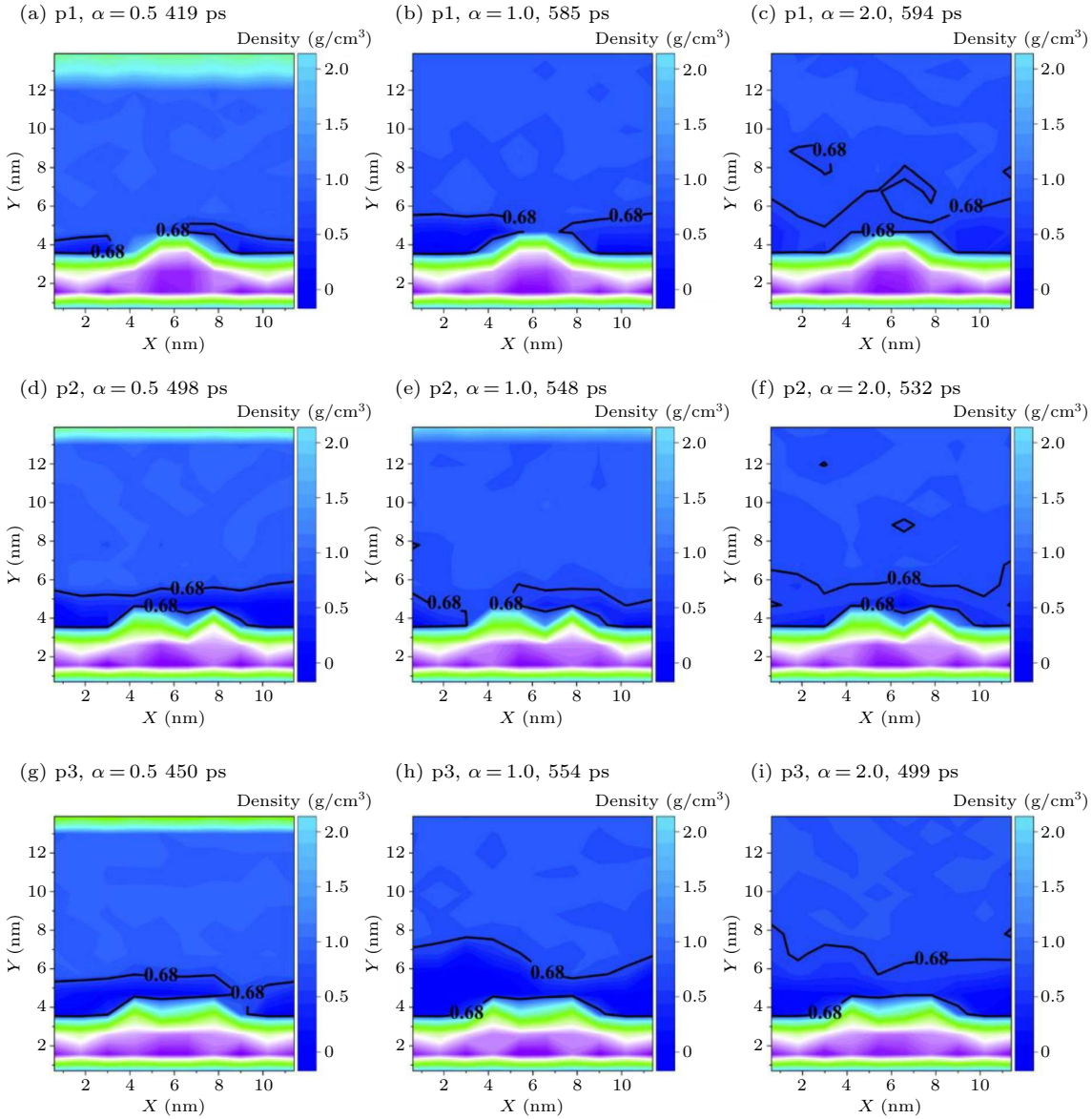


Fig. 6. Density distribution cloud map.

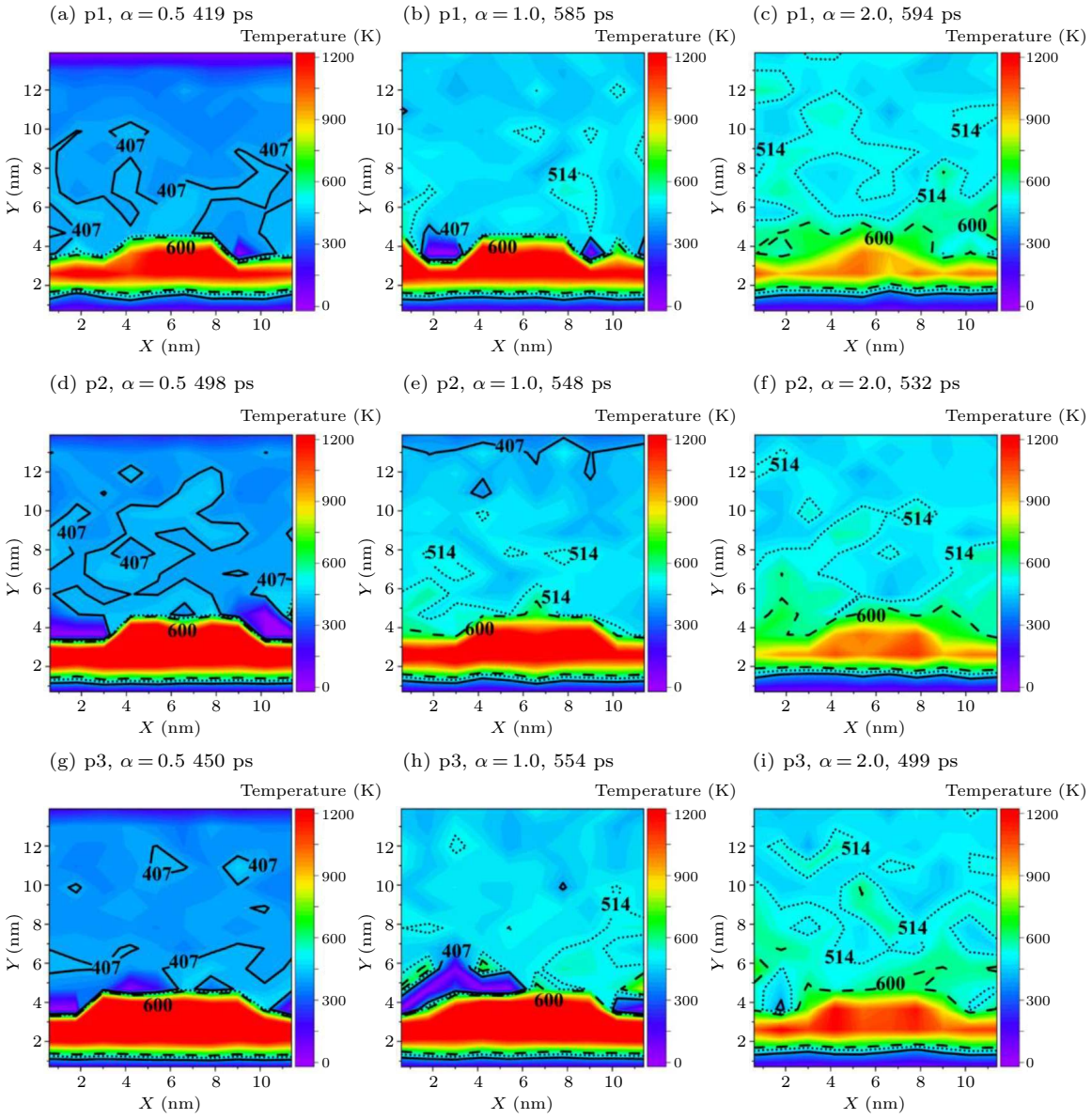


Fig. 7. Temperature distribution cloud map.

The elevated temperature of the liquid near the bottom of the system is attributed to the transfer of thermal energy from the solid substrate to the liquid across the solid–liquid interface. This interfacial heat transfer raises the local temperature in the adjacent liquid region.[44,45] Once the liquid molecules acquire sufficient energy, their kinetic energy can exceed the intermolecular attraction forces, leading to evaporation. Under the same heat flux density, the combined effects of surface protrusion geometry and surface wettability collectively determine the liquid-phase transition behavior and the preferential sites of bubble nucleation. As the number of surface protrusions increases, the curvature variation is enhanced, making the rib sidewalls regions of concentrated heat and preferred bubble-generation sites. This promotes a more vigorous phase-transition process.[46] In contrast, enhanced wettability tends to inhibit bubble expansion, resulting in a more localized and stable evaporation process. Preferential bubble nucleation along the rib sides was observed under all three wettability conditions. This phenomenon arises from the coupling of multiple factors, including geometric enhancement, localized heat accumulation, and nitrogen-assisted nucleation.

3. Regression analysis of influencing factors

To further evaluate the relative influence of surface wettability and the number of sinusoidal protrusions on the phase-change heat transfer process, this study employs regression analysis based on established statistical methods.[47,48] Since the magnitudes of these variables differ substantially, direct regression would introduce scale imbalance and distort the results. Therefore, as a preparatory step for normalization and comparative analysis, the effective heat transfer area was first calculated as the specific surface area relative to the total volume of the copper substrate. Subsequently, all data were stan-

dardized using the Z-score method, defined as

$$Z = \frac{X - \mu}{\theta}, \tag{9}$$

where X represents the original data, μ is the sample mean, and θ denotes the sample standard deviation. The normalized results are obtained as follows.

Table 3. Number of protrusions and standardized results.

Number of protrusions	1	2	3	4	5
Standardised results	−1.4255	−0.7496	0.1562	0.5950	1.4238

The wetting coefficient values were not subjected to normalization, as they represent intrinsic parameters within the hydrophilic–hydrophobic correction formulation. These coefficients possess direct physical significance and are not intended as fitted variables within the regression model. Standardization could compromise their physical interpretability. Therefore, the original wettability parameter was retained to more accurately reflect its actual role in the phase-transition process.

For the simulation results, two key indicators were selected for regression analysis: (i) the simulation time required for the top control plate to reach a specified height, reflecting the rate of phase change and the responsiveness of the boiling process. This indicator primarily compares the rate of liquid evaporation and phase transition under different simulation conditions; and (ii) the height of the top plate at a fixed time point, representing the intensity of phase change and cumulative heat transfer, thereby assessing whether the phase transition is sufficiently developed and extensive.

The reference time corresponds to the condition exhibiting the fastest phase transition, namely, the system with five sinusoidal protrusions on a hydrophilic surface. In the height-based analysis, the selected reference height is defined as the point where the liquid film is completely detached from the surface and has reached 20 Å above the top of the protrusion, beyond the effective range of intermolecular forces. This condition represents the slowest phase transition among the simulated cases, i.e., a hydrophilic surface with only one protrusion.

These two indicators are used to evaluate (i) the time required to complete the phase transition and (ii) the adequacy of the phase-transition process. To ensure consistency and comparability across systems, Z-score normalization was applied to the simulation results. Linear regression analysis was then performed according to

$$\gamma = \delta_0 + \delta_1 \alpha + \delta_2 p + \varepsilon, \tag{10}$$

$$\varepsilon_i = \gamma_i - (\delta_0 + \delta_1 \alpha + \delta_2 p), \tag{11}$$

$$\mathrm{RSS} = \sum_{i=1}^{n} \left[\gamma_i - (\delta_0 + \delta_1 \alpha + \delta_2 p)\right]^2, \tag{12}$$

where γ is the dependent variable, α represents the effect of wettability, and p represents the number of sinusoidal protrusions. δ_0 is the intercept term, δ_1 and δ_2 are regression coefficients, and ε denotes the error term. RSS refers to the residual sum of squares.

Next, a matrix was constructed using the normalized simulation times required to reach a given height, and the regression analysis was conducted using the least-squares method as

$$\beta = (B^{\mathrm{T}} \cdot B)^{-1} \cdot B^{\mathrm{T}} \cdot \gamma. \tag{13}$$

The regression yielded the following coefficients: $\delta_0 \approx 0.101$, $\delta_1 \approx -0.087$, and $\delta_2 \approx -0.845$. To evaluate the model's goodness of fit, the coefficient of determination R^2 was calculated as

$$R^2 = 1 - \frac{\sum_{i=1}^{n} (\gamma_i - \hat{\gamma}_i)^2}{\sum_{i=1}^{n} (\gamma_i - \bar{\gamma})^2}, \tag{14}$$

yielding $R^2 = 0.768$, indicating that the linear regression model provides a relatively weak fit.

A separate linear regression based on the height reached at a fixed time produced $\delta_0 \approx -0.268$, $\delta_1 \approx 0.229$, $\delta_2 \approx 0.816$, with $R^2 = 0.736$. Although slightly lower than the previous case, these results suggest that the number of sinusoidal protrusions exerts a more significant influence on the final height achieved.

Overall, the linear regression demonstrates limited predictive accuracy and fails to fully capture the nonlinear relationships among variables. Accordingly, a second-order polynomial regression model was employed to analyze the simulation time required to reach the same height

$$\begin{aligned} \hat{\gamma} = {} & -1.5176 + 3.5578\alpha - 0.5710p \\ & -1.4173\alpha^2 - 0.2403\alpha p, \end{aligned} \tag{15}$$

where α represents the wettability effect and p denotes the number of protrusions. The coefficient of determination for the polynomial regression was $R^2 = 0.925$, substantially higher than that of the linear models, indicating a much improved fit.

Figure 8 displays the fitted surface constructed from the regression model alongside the simulation data. Most points align closely with the fitted surface, confirming the model's reliability. The positive first-order coefficient of wettability and the negative second-order term indicate that moderate increases in wettability initially enhance phase transition, but excessive hydrophilicity eventually suppresses it.

The regression surface exhibits a noticeable flattening near both the center and the boundaries, while the negative

interaction term suggests that an optimal combination of wettability and protrusion number yields the most efficient phase-transition performance. Nevertheless, the protrusion structures alone do not substantially accelerate the phase-change rate.

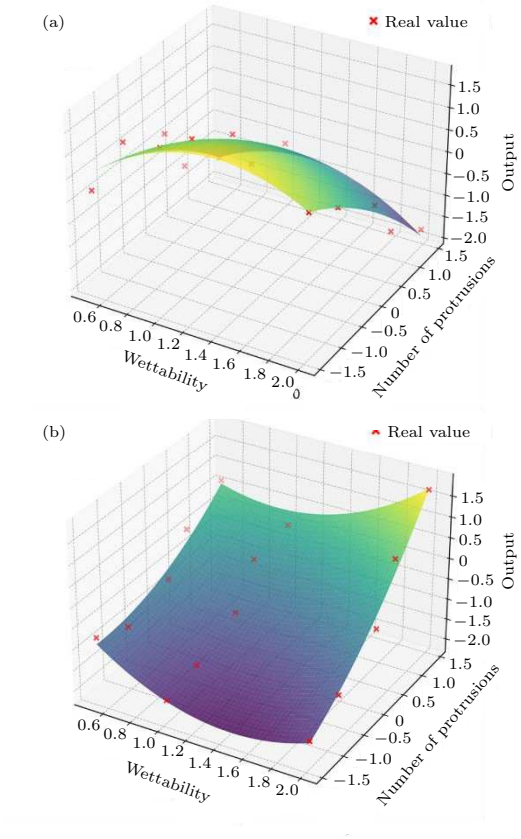


Fig. 8. Second order regression fitting surfaces.

The coefficient of determination (R^2) obtained from the second-order regression analysis based on the dataset of top plate heights at the same time point is 0.940, indicating an excellent fit. The corresponding second-order regression surface is described by

$$\hat{\gamma} = 1.0703 - 2.9258\alpha + 0.2908p + 1.2270\alpha^2 + 0.4577\alpha p. \quad (16)$$

The fitted surface exhibits a clear upward trend and distinct nonlinear characteristics, suggesting that both variables exert complex nonlinear effects under this evaluation criterion. The surface closely follows the distribution of the data points, implying that the model effectively captures the overall trend. Although both regression equations contain statistically insignificant terms based on t-tests and p-values, the second regression model demonstrates a higher coefficient of determination and better predictive performance.

The regression results further reveal that wettability exhibits an optimal range: excessive hydrophilicity tends to suppress the phase change process. In contrast, an increase in the number of protrusions positively influences the intensity of the phase transition and enhances heat accumulation. Overall, the interaction term reflects the coupled effects of wettability and protrusion density. Enhancing wettability alone delays nucleation, whereas simultaneously increasing protrusion density markedly increases the number of heterogeneous nucleation sites provided by the surface. This interaction mitigates or even reverses the delay caused by high wettability. The negative and positive coefficients of the interaction term corroborate this physical mechanism–neither factor dominates entirely; instead, they counterbalance one another. Improving a single factor alone may not sustainably enhance phase transition performance. Rather, the optimal outcome is achieved through the coordinated balance between the two factors.

Although the effects of various influencing factors have been analyzed, the limited sample size constrains the generalizability of the conclusions. Further simulations and analyses with expanded datasets and additional variables are required to validate this methodology and enhance the robustness and reliability of the research findings.

4. Conclusion

Based on molecular dynamics simulations, several models were established in this study to investigate the effects of insoluble gas, surface wettability, and nanoscale structures on the phase transition process. Correlation analyses between wettability and nanostructures were further conducted to evaluate their combined influence under different conditions. The main conclusions are summarized as follows.

(i) In the presence of nitrogen, surface wettability constrains the phase transition process and reduces the boiling rate. Although hydrophilic surfaces delay the onset of boiling, they ultimately enhance the overall phase transition rate.

(ii) Increasing the number of nanostructures significantly promotes the phase transition process and advances the onset of boiling. The phase change typically initiates within the grooves along the sides of the protruding ribs.

(iii) Regression analysis indicates that wettability exhibits an optimal range: both excessive hydrophilicity and excessive hydrophobicity are detrimental to the phase transition process. Moreover, wettability demonstrates a positive synergistic effect with the protrusion structures, which further facilitates the phase transition.

(iv) Due to equipment limitations, a broader combination of influencing factors was not considered in this simulation. Future studies should incorporate a more comprehensive set of parameters. In addition, the limited number of data points restricted the analysis to second-order regression, which may not fully capture all potential interactions and nonlinear trends.

Acknowledgment

This work was supported by the National Natural Science Foundation of China (Grant No. 52176077).

References

[1] Chen Y J, Zou Y, Sun D L, Wang Y and Yu B 2018 *Int. J. Heat Mass Transf.* **118** 1143
[2] Hajebzadeh H, Abedini E, Adibi P and Hosseini M 2023 *Int. Commun. Heat Mass Transf.* **146** 106890
[3] Zhang P, Zhou L, Jin L, Zhao H and Du X 2019 *Appl. Phys. A* **125** 142
[4] She X, Shedd T A, Lindeman B, *et al.* 2016 *Int. J. Heat Mass Transf.* **95** 278
[5] Hong S, Jiang S, Hu Y, Dang C and Wang S 2019 *Int. J. Heat Mass Transf.* **136** 235
[6] Dong L N, Quan X J and Cheng P 2012 *Int. J. Heat Mass Transf.* **55** 4376
[7] Seyf H R and Zhang Y 2013 *Int. J. Heat Mass Transf.* **66** 613
[8] Yin X, Hu C, Bai M and Lv J 2019 *Int. J. Multiphase Flow* **115** 9
[9] Hung T C, Yan W M, Wang X D and Chang C Y 2012 *Int. J. Heat Mass Transf.* **55** 2559
[10] Esfe M H, Yan W M, Akbari M, Karimipour A and Hassani M 2015 *Int. Commun. Heat Mass Transf.* **68** 248
[11] Nagayama G, Tsuruta T and Cheng P 2006 *Int. J. Heat Mass Transf.* **49** 4437
[12] Nagayama G and Cheng P 2004 *Int. J. Heat Mass Transf.* **47** 501
[13] Chen Y J, Zou Y, Wang Y, Han D X and Yu B 2018 *Int. Commun. Heat Mass Transf.* **98** 135
[14] Chen Y, Li J, Yu B, Sun D, Zou Y and Han D 2018 *Langmuir* **34** 14234
[15] Liu R and Liu Z 2019 *Int. J. Heat Mass Transf.* **143** 118534
[16] Hens A, Agarwal R and Biswas G 2014 *Int. J. Heat Mass Transf.* **71** 303
[17] Li B, Gu Y and Chen M 2017 *Exp. Fluids* **58** 164
[18] Baidakov V G 2016 *J. Chem. Phys.* **144** 074502
[19] Wu L F, Tang Y Z, Ma L X, Feng S Y and He Y 2022 *Int. J. Therm. Sci.* **171** 107212
[20] Yastrebov V A, Anciaux G and Molinari J F 2014 *Tribol. Lett.* **56** 171
[21] Wang S, Wu L F, Tang Y Z and He Y 2022 *Coatings* **12** 1943
[22] Mishin Y, Mehl M J, Papaconstantopoulos D A, Voter A F and Kress J D 2001 *Phys. Rev. B* **63** 224106
[23] Berendsen H J C, Grigera J R and Straatsma T P 1987 *J. Phys. Chem.* **91** 6269
[24] Kusalik P G and Svishchev I M 1994 *Science* **265** 1219
[25] Ryckaert J P, Ciccotti G and Berendsen H J C 1977 *J. Comput. Phys.* **23** 327
[26] Hockney R W and Eastwood J W 1988 *Computer Simulation Using Particles* (New York: CRC Press)
[27] Jorgensen W L, Maxwell D S and Tirado-Rives J 1996 *J. Am. Chem. Soc.* **118** 11225
[28] Kaminski G A, Friesner R A, Tirado-Rives J and Jorgensen W L 2001 *J. Phys. Chem. B* **105** 6474
[29] Rafiee J, Mi X, Gullapalli H, Thomas A V, Yavari F, Shi Y, Ajayan P M and Koratkar N A 2012 *Nat. Mater.* **11** 217
[30] Plimpton S 1995 *J. Comput. Phys.* **117** 1
[31] Kaye G W C and Laby T H 1986 *Tables of Physical and Chemical Constants* 15th edn. (New York: Longman) p. 219
[32] Deng W, Ma S, Li W, Liu H and Zhao J 2022 *Int. J. Heat Mass Transf.* **191** 122856
[33] Stukowski A 2010 *Model. Simul. Mater. Sci. Eng.* **18** 015012
[34] Humphrey W, Dalke A and Schulten K 1996 *J. Mol. Graph.* **14** 33
[35] Langmuir I 1918 *J. Am. Chem. Soc.* **40** 1361
[36] Hanaor D A H, Ghadiri M, Chrzanowski W and Gan Y 2014 *Langmuir* **30** 15143
[37] Israelachvili J N 2011 *Intermolecular and Surface Forces* (San Diego: Academic Press)
[38] Zhong X, Yu J, Guo X and Saeed M 2018 *Nucl. Eng. Des.* **328** 301
[39] Luo Q Q and Yang J M 2015 *Chin. Phys. B* **24** 096801
[40] Jia J Q, Dang L X and Miller J D 2018 *Physicochem. Probl. Miner. Process.* **54** 89
[41] *The Engineering Toolbox, "Gases–Density"*, accessed January 27, 2019, available at https://www.engineeringtoolbox.com/gas-density-d_158.html
[42] Tanaka M, Girard G, Davis R, Peuto A and Bignell N 2001 *Metrologia* **38** 301
[43] Liu J T, Peng X F and Yan W M 2007 *Int. J. Heat Mass Transf.* **50** 1855
[44] Li Z, Tan X, Fu Z, Liu L and Yang J Y 2023 *Phys. Chem. Chem. Phys.* **25** 6746
[45] Oztop H F, Estelle P, Yan W M, Al-Salem K, Orfi J and Mahian O 2015 *Int. Commun. Heat Mass Transf.* **60** 37
[46] Lu G, Wang X D and Yan W M 2017 *Int. J. Heat Mass Transf.* **108** 2253
[47] Draper N R and Smith H 1998 *Applied Regression Analysis* 3rd edn. (New York: Wiley)
[48] Neter J, Kutner M H, Nachtsheim C J and Wasserman W 1996 *Applied Linear Statistical Models* (Chicago: Irwin)